High spatial and energy resolution electron energy loss spectroscopy of the magnetic and electric excitations in plasmonic nanorod oligomers

GRACE PAKELTIS,[1] ⓘ ENZO ROTUNNO,[2] ⓘ SIAMAK KHORASSANI,[3] ⓘ DAVID A. GARFINKEL,[1] ROBYN COLLETTE,[1] CLAIRE A. WEST,[4] ⓘ SCOTT T. RETTERER,[5] JUAN CARLOS IDROBO,[5] ⓘ DAVID J. MASIELLO,[3,4] ⓘ AND PHILIP D. RACK[1,5,*] ⓘ

[1]*Department of Materials Science and Engineering, University of Tennessee, Knoxville, TN 37996, USA*
[2]*CNR-NANO Via G. Campi 213/a, I-41125, Modena, Italy*
[3]*Department of Materials Science and Engineering, University of Washington, Seattle, WA 98195, USA*
[4]*Department of Chemistry, University of Washington, Seattle, WA 98195, USA*
[5]*Center for Nanophase Materials Sciences, Oak Ridge National Laboratory, Oak Ridge, TN 37831, USA*
[*]*prack@utk.edu*

Abstract: We leverage the high spatial and energy resolution of monochromated aberration-corrected scanning transmission electron microscopy to study the hybridization of cyclic assemblies of plasmonic gold nanorods. Detailed experiments and simulations elucidate the hybridization of the coupled long-axis dipole modes into collective magnetic and electric dipole plasmon resonances. We resolve the magnetic dipole mode in these closed loop oligomers with electron energy loss spectroscopy and confirm the mode assignment with its characteristic spectrum image. The energy splitting of the magnetic mode and antibonding modes increases with the number of polygon edges (n). For the n=3-6 oligomers studied, optical simulations using normal incidence and s-polarized oblique incidence show the respective electric and magnetic modes' extinction efficiencies are maximized in the n=4 arrangement.

1. Introduction

The search for metamaterials that exhibit negative permittivity and permeability in the visible spectrum has led to the exploration of architectures that support coupled plasmonic elements. While standard split ring resonators (SRR) have been extensively studied and shown to be extendable to near infrared frequencies, [1] pushing to higher frequencies is challenging. Cut SRR geometries or coupled nanospheres have been shown to be a viable solution for higher frequency applications [2]. However, while optical and magnetic properties of coupled nanospheres [3–5] and disks [6,7] have been studied more comprehensively, anisotropic bi-spheres [8] and rods have stronger polarizability and thus afford a greater opportunity for demonstrating high frequency negative permeability and permittivity. Additionally, pairs of parallel nanorods have been shown to exhibit anti-symmetric resonances that generate a magnetic field, which has also been explored for negative permeability. [9]

Plasmonic oligomers, cyclic assemblies of plasmonic nanoparticles made up of high aspect ratio nanorods, provide another geometry for high frequency collective electric and magnetic responses that are, in addition, spectrally distinct. The hybridized energies of such oligomers depend on the edge length, gap size, and number of edges. The magnetic and electric dipole modes of triangular nanorod oligomers have been studied previously [10] as have coupled symmetric and asymmetric pairs of triangular nanorod oligomers. [11] While the hybridization of

symmetric oligomers leads to the expected low energy all in-phase magnetic dipole configuration and the maximum out-of-phase high energy configuration, asymmetry modifies the hybridization. For instance, as shown in simple dimer-coupling [12], asymmetric rod length and nanorod composition effect the in-phase and out-of-phase mode splitting. In nanorod trimers [11] and nanoparticle tetramers [13] slight shifts in one of the mer positions/size can affect the magnetic dipole scattering cross-section and lead to a Fano resonance based on the interaction of the magnetic dipole with the electric dipole. Nevertheless, a comprehensive investigation of the hybridization of higher order oligomers composed of high aspect ratio nanorods is still lacking. In the following, we nanofabricate a series of such oligomers ranging from trimers to hexamers and study their spectral and spatial plasmonic responses with high-resolution monochromated and aberration corrected electron energy loss spectroscopy (EELS). Complementary electron beam and optical simulations are used to elucidate our experimental observations.

2. Methods

2.1. Nanorod polygon fabrication

The nanorod polygons were fabricated via electron-beam lithography (JEOL 9300FS) using a lift-off process. While the original lithography pattern is rectangular, no proximity correction is applied and thus the rod ends are slightly rounded. While slight field concentrations would likely emerge at the corners for rectangular rod ends, the hemispherical ends versus rectangular ends are not expected to affect the results discussed below. A 300 μm Si wafer with 30 nm of low pressure chemical vapor deposition (LPCVD) SiN_x is spin coated with an e-beam resist, PMMA 495 A4, and exposed. Following electron-beam exposure, the pattern was then developed using methyl isobutyl ketone:isopropyl alcohol (IPA) (1:3) for 50 s. 25 nm of Au was sputter deposited via DC magnetron sputtering onto the substrate followed by soaking in a heated NMP bath for 15 min, sonicating in NMP and acetone for 10 min, and rinsing with IPA and deionized water. The backside of the wafer was then spin coated with P20 and S1818 and exposed using photolithography to create the windows for backside etching. Reactive ion etching is used to remove the backside nitride layer and the wafer is subsequently submerged in a heated KOH bath to etch away the exposed portion of Si substrate, stopping on the SiN_x windows to create the TEM grid edges.

2.2. Electron energy loss spectroscopy

Low-loss EEL spectra and spectrum images were taken using a Nion aberration-corrected high energy resolution monochromated EELS-STEM (HERMES) operated at an accelerating voltage of 60 kV. [14,15] The convergence and collection semiangles used for the spectrum acquisition were 30 and 15 mrad, respectively. The energy resolution (full width at half-maximum of the zero-loss peak) was approximately 20 meV. The EEL spectra presented were normalized to the zero-loss peak.

2.3. Optical extinction and electron beam simulations

Optical and electron energy loss simulations were carried out using discrete dipole approximation (DDA) [16] and electron-driven DDA [17] (e-DDA), respectively. These numerical methods offer flexibility for irregular shapes and are well suited to simulate oligomers with the different polygon shapes studied here. For all EELS simulations, the shape dimensions and orientations have been determined based on their experimental counterparts; the substrate is not included for computational efficiency. The primary electron beam energy was set to be 60 keV, and the impact parameter was chosen as 5 nm. All oligomers eDDA spectra were calculated in vacuum for computational efficiency. The silicon nitride substrate present in the experiment has no resonances and is dispersionless in the energy range measured. Thus, the only effect the substrate

will have on the oligomers is an overall red-shift of the resonances due to the image effect. The approximate 60 meV shift applied to the spectra is on the order of the expected red-shift due to the image effect and is applied to account for this effect and better compare the spectra. All electric and magnetic field maps were generated in a plane parallel to the nanostructure located in the near-field above the structure.

2.4. Boundary element method calculations

In our simulations, we computed the plasmon response function by solving the Maxwell's equations in the quasistatic approximation through the boundary element method [18] as implemented in MNPBEM toolbox. [19] As we are mainly interested in the symmetries of the different plasmon modes, we found it convenient to seek the eigenvalues and vectors of the surface derivative of the Green function, following the approach shown in Boudarham and Kociak. [20] This approach has the advantage that the solutions can be interpreted in terms of eigenmodes, which, in case of plasmonic nanoparticles, are precisely given by the surface plasmons. [21] The electrostatic potential associated with each plasmonic mode $V(r,\varphi)$ has then been fitted according to the multipolar expansion $V(r,\varphi) = \sum_{m=-\infty}^{\infty} f_m(r)e^{im\varphi}$. The analysis of the multipole moment coefficients $c_m = \int |f_m(r)|^2 dr$ is a useful tool to investigate the azimuthal symmetry of the plasmonic mode in a quantitative way.

Because the size of the system considered in this paper is beyond the validity limit of the quasistatic approximation, we accounted for retardation effect solving the full Maxwell equations in some selected cases (see Supplement 1) finding that the symmetry of the calculated modes is retained when retardation effects are accounted for.

As for the dielectric function of gold we use tabulated values extracted from spectroscopic ellipsometry measurements. [22] The effect of the SiN membrane supporting the metal structures has been modeled as the average between the tabulated dielectric function of SiN [23] and the vacuum.

3.   Results and discussion

A series of oligomers composed of high aspect ratio gold nanorods are lithographically patterned with varying numbers of edges (n=3-6), gap length, and edge length. High spatial and energy resolution EEL spectrum images are measured, and the combined spectra and spectrum images clearly reveal the nature of the various resonant modes that are active. Note that for polygons where n is even, the highest energy mode has n antibonding vertices, whereas for odd number of edges, the maximum number of antibonding modes is *n-1*. As n increases, the number of normal modes increases and the energy splitting of the magnetic all head-to-tail configuration and maximum head-head/tail-tail configuration increases. Depending on the resultant configuration, different net magnetic and electric fields emerge.

To characterize the oligomers' hybridization, we synthesize oligomers consisting of high aspect ratio gold nanorods with approximately the same rod length (540 nm), width (75 nm), and thickness (25 nm) and measure high spatial and energy resolution EEL spectrum images at a vertex of each polygon. Notably, the high aspect ratio minimizes coupling of the transverse/short axis surface plasmon resonance (SPR), which, for this rod dimension has an energy on the order of 2.1 eV, whereas the long axis mode has an energy of ~650 meV. Figure 1(a) displays normalized experimental and simulated electron-driven discrete dipole approximation (e-DDA) spectra taken near a nanorod tip for each oligomer (see inset for STEM image and location for each spectrum), which illustrates the resulting hybridization of the coupled rods. Note, the e-DDA spectra have all been shifted 60 meV to lower energy to better align with the experimental spectra; the slight shift to higher energy in the simulated spectra is due to the SiN_x substrate, which was not included in the simulations. Also included are the energies (vertical lines) of the boundary element method (BEM) simulated SPR modes. The trimer, as illustrated previously, [10,11] consists

of two non-degenerate modes, which are clearly observed in the spectrum. For the tetramer, pentamer, and hexamer, however, intermediate peaks emerge between the magnetic mode and the high-energy antibonding configuration. Figure 1(b) is a plot of the experimental peak positions of the magnetic mode, the maximum antibonding configuration, and the energy difference illustrating that the total hybridization splitting increases progressively as *n* increases. Figure 1(c) shows spectrum images of the tetramer magnetic dipole mode (top), electric dipole mode (middle), and high-energy mode (bottom) consisting of all antibonding vertices, respectively (see Supplemental Fig. S2 for *n*=3,5,6 spectrum images). As expected, the spectrum images confirm the head-to-tail or bonding mode with the near zero EEL intensity in the gap center for the magnetic mode. Furthermore, the high energy antibonding head-to-head/tail-to-tail configuration is characterized by a gap center that has high EEL intensity. The intermediate energy spectrum image is characterized by a mixture of the two modes, and as will be described below, this mode
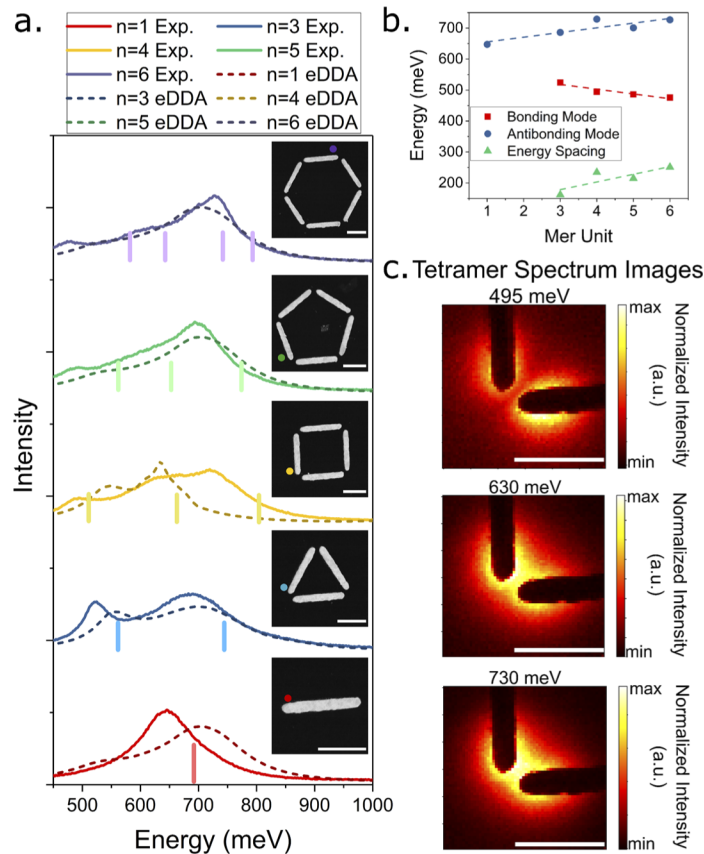

Fig. 1. a. Experimental and simulated spectra taken at the nanorod tip for a single rod and n=3-6 oligomers. Vertical lines indicate normal modes calculated for each oligomer. Inset HAADF images illustrate the location of the beam for the spectra acquisition. b. Peak energies for the electric and magnetic dipoles as a function of the number of edges in the regular polygonal oligomers. Also plotted is the energy splitting between the high and low energy modes illustrating increased splitting as the number of edges increases. c. Spectrum images are measured at a vertex of the tetramer and are filtered to illustrate the magnetic dipole (495 meV), the intermediate electric dipole mode (630 meV), and the full antibonding mode (730 meV). Scale bar=300 nm.

is the electric dipole mode of the tetramer and consists of half of the vertices with bonding and half with antibonding characteristics.

In order to elucidate and confirm the symmetry of the different plasmonic modes, information that cannot be directly extrapolated from spectrum images, [24,25] we performed BEM numerical simulations (see Methods for details). While the oligomer geometries are outside the quasistatic limit assumed in the BEM model, the energies of the normal modes agree well with the experimental results and help reveal the general hybridization trends of the oligomers.

We start from the case of the trimer. In Figs. 2(a)–2(c), we plot the induced charge distributions of the SPRs that have energy in the 300-1000 meV range. The mode energies resulting from the simulation are in good agreement with experiment, with slight differences attributed to small variations in the experimental nanorod shapes. As expected, the lowest energy mode [Fig. 2(a)] is characterized by all head-to-tail coupling of the longitudinal dipoles of the rods. The resulting plasmonic potential is a pure hexapole [Fig. 2(d)], which is confirmed by the multipolar expansion reported in Fig. 2(g). The second peak in the spectrum is two degenerate modes [Figs. 2(b)–2(c)]. This mode [26] can be described as the strong excitation of the dipole modes of two adjacent rods in a head-to-head, or antibonding configuration, plus a small excitation of the quadrupolar mode of the opposite rod to ensure charge neutrality. The two modes are rotated by a 120° angle, reflecting the symmetry of the polygon, but are otherwise identical as it is apparent from the multipole moment decomposition.
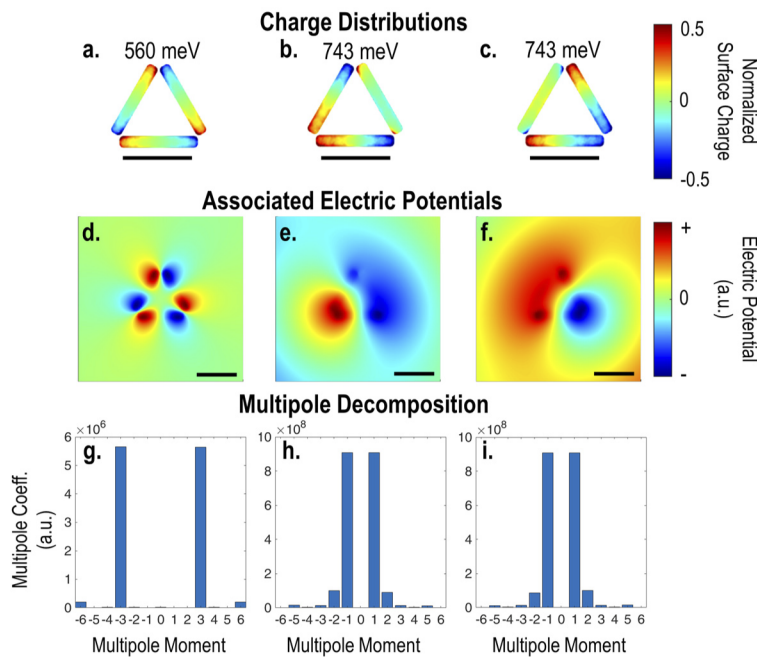

Fig. 2. The induced charge distributions (a-c), the associated electric potential (d-f) and its multipolar decomposition coefficients (g-i) of the first 3 plasmonic modes of the n=3 polygon. Scale bar = 500 nm.

Small imperfections of the structure, such as the edge perturbations or small differences in the edge or gap length, can slightly relax the degeneracy of this electric dipole mode and thus slightly split the two modes. Additionally, the radiation damping in the magnetic mode is suppressed relative to the bright electric dipole mode. As a consequence, the higher energy peak of the experimental spectrum is broader than the lowest energy one. The associated electric field is a

dipole, with a small quadrupolar component required to compensate for the odd symmetry of the particle [Figs. 2(e)–2(f)and Figs. 2(h)–2(i)].

Any linear combination of two degenerate modes is also a mode with the same energy, therefore, it is interesting to note the shape of the two trivial combinations, i.e. the sum and the difference, of the two modes. As reported in Fig. 3, the difference gives an equivalent mode rotated by 120° with respect to both parent modes, completing the angular series. The sum mode is very simple from a geometrical point of view, as it can be understood as the flipping of one rod in the lowest energy mode (the bottom rod in this representation) to form two antibonding configurations and one bonding configuration. These results hold true every time we encounter a set of degenerate modes, therefore in the following we will only show one of the degenerate modes with the simplest geometrical shape.
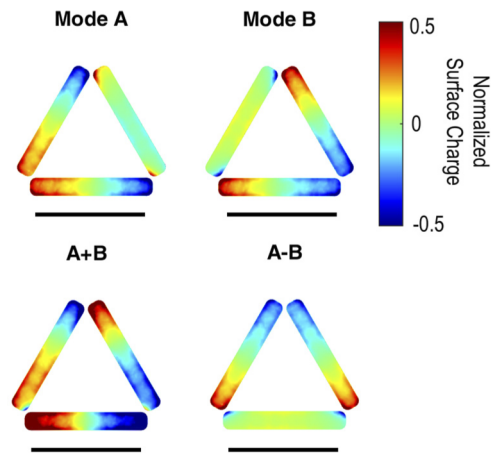

Fig. 3. Linear combinations of the two 743 meV modes (A and B) of the trimer. Scale bar = 500 nm

In Fig. 4, we show the induced surface charge distributions of the plasmonic modes (and their associated induced potentials) that have energy in the 300-1000 meV range computed for all the oligomers with n=3-6. The gray star in the top right corner denotes a set of degenerate modes for which only one representation is reported. The complete list of modes can be found in the Supplemental Figs. S3, S4, and S5. Again, the simulations are in good agreement with the experiments. Note, as the size of the structures are large relative to the excitation wavelength, the quasistatic approximation begins to fail, and causes the observed blue-shift of the energies relative to experiment.

The lowest energy mode of each polygon [Figs. 4(a), 4(c), 4(f), and 4(i)] is always a multipole with the same rotational symmetry of the oligomer. As expected, it is characterized by all head-to-tail coupling of the dipole modes of the rods and results in the circulating current and thus a strong magnetic field perpendicular to the plane of the oligomer. The subsequent modes are ordered in the usual way, with the electric dipole being the lowest energy configuration followed by the quadrupole and the higher electric multipoles.

The shape of the different modes can be understood by simple geometrical arguments. In order to induce an electric dipole, the charge density should be mirrored on one side of the metal structure. This is achieved by flipping, where allowed by the particle symmetry, all the dipoles of the constituent nanorods on one side of the structure. Following this argument, higher order multipoles are obtained by flipping dipoles on the opposite side of a mirror plane or alternating them along the perimeter of the polygon (see for example the hexapole mode of the n=6 polygon).
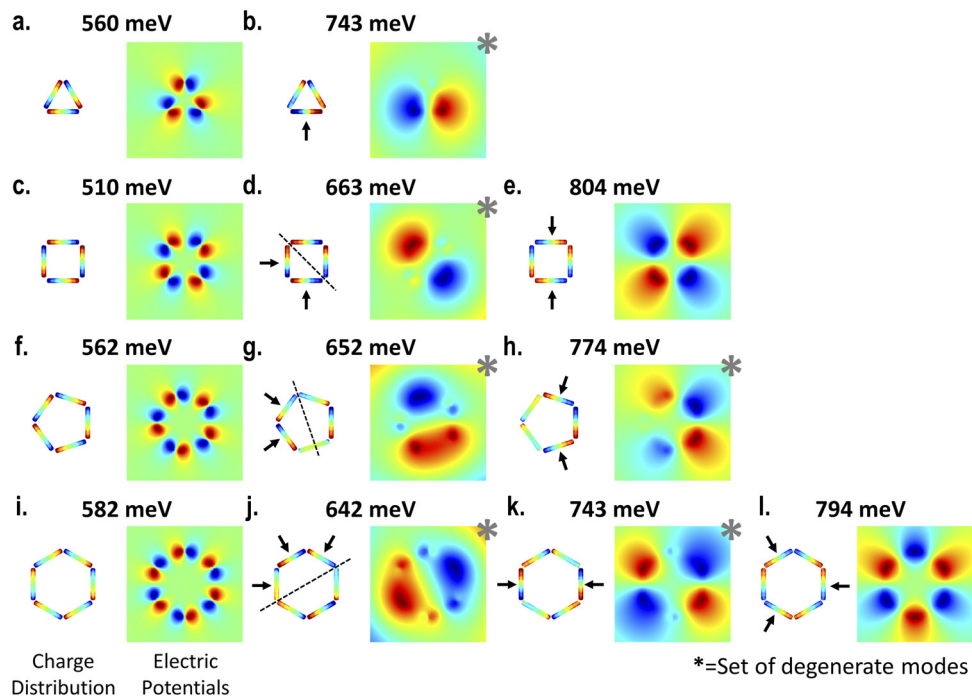
Fig. 4. The charge density distributions and the associated electric potentials computed for the LSPRs of the n=3 polygon (a and b), the n=4 polygon (c-e), the n=5 polygon (f-h) and the n=6 polygon (i-l). The modes marked with the grey star are pairs of degenerate modes for which only a single representation have been reported. The higher energy modes of each polygon can be derived from the lowest energy mode by flipping the orientation of the dipole modes of some of the nanorods (marked with the black arrows).

The flipped dipoles have been marked with black arrows and the mirror planes with dashed lines. Note the net electric dipole is aligned along the axis of symmetry of the mirror plane.

To further explore hybridization trends in nanorod oligomers, tetramers with various gap spacing are investigated. Studies on trimers composed of spherical particles have shown that increasing the gap size decreases the energy of both the electric and magnetic hybridized dipole modes and total splitting due to reduced capacitive coupling [27]. Fig. 5(a) shows the EEL spectra and Fig. 5(b) the energy positions and energy difference in the two modes as a function of gap spacing (see Supplemental Fig. S6 for spectrum images). The spectra also show that as the gap length increases, the energy splitting decreases linearly from 235 meV to 95 meV over the gap range studied [Fig. 5(b)]. Similar to the n>3 polygons in Fig. 1(a), an intermediate mode is discernible in gaps below 100 nm. As the gap increases above 100 nm, the intermediate mode that is distinguishable at smaller gaps, overlaps significantly with the high energy mode and becomes indistinguishable. At larger gap distances, the spectrum will approach the single rod spectrum.

The effect of rod length on coupling is also studied. Nanorod tetramers are synthesized with a rod length ranging from 345 nm to 1100 nm with a constant gap spacing of ~50 nm. The spectra are shown in Fig. 5(c), and clearly show the splitting into the magnetic and high-energy maximum antibonding mode, which are confirmed by the spectrum images (see Supplemental Fig. S7). As expected, Fig. 5(d) shows a linear blue-shifting of the magnetic and high-energy modes as the rod length decreases [28]. Additionally, a clear increase in the magnitude of the energy splitting is also observed as the rod length decreases. Note the higher energy quadrupolar
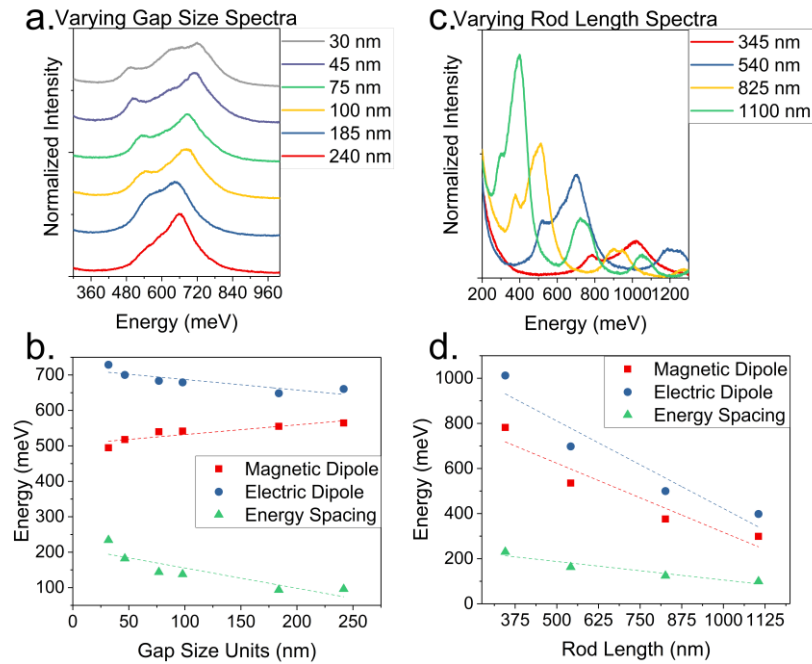
Fig. 5. EEL data for tetramer oligomers with varying gap size and edge length. a) Spectra taken at the rod tip for gap sizes 30 nm, 45 nm, 75 nm, 100 nm, 185 nm, and 240 nm. b) Peak energies for the low and high energy modes and energy splitting of the modes as a function of gap size. c) Spectra taken at the rod tip for rod lengths 345 nm, 540 nm, 825 nm, and 1100 nm. d) Peak energies for the low and high energy modes and energy splitting of the modes as a function of rod length.

mode hybridization is also evident in Fig. 5(d) at higher energy for all but the 300 nm edge length tetramer as its quadrupolar mode is shifted to beyond what is measured.

Optical DDA simulations are used to determine the extinction efficiencies associated with the modes of the oligomers. Figure 6(a) is a plot of the simulated extinction efficiency for each oligomer for oblique s-polarized excitation where the magnetic field is oriented perpendicular to the oligomer plane (note the specific polarizations for each oligomer next to each spectrum). The extinction efficiency peak confirms the magnetic field coupling of the light field to the oligomers' magnetic modes. The excitation of the n=3 mode is expected to be a bright mode, note that the high energy modes of the other oligomers are also excited under this polarization. Electric field maps of these excited modes, confirm that these modes are the full antibonding modes, as previously illustrated in Figs. 4(b) 4(e), 4(h), and 4(l). Thus, while these modes are expected to be dark, phase retardation effects are apparently operative when the wavevector is aligned along the plane of the oligomer. Figure 6(b) is a plot of the magnetic mode extinction efficiency as a function of *n*, which illustrates that the extinction efficiency is a maximum for the *n*=4 oligomer. A circular current loop generates a resultant magnetic field perpendicular to the loop according to the Biot-Savart Law. The SPR plasmon frequency is set by the monomer length and the maximum magnetic moment is dictated by μ=iA, where i is the current and is governed by plasmon damping/losses and A is the oligomer area. As the number of edges increases, the oligomer area increases. Consequently, the peak in the extinction coefficient for the n=4 oligomer suggests that the losses in the SPR are likely at the oligomer gaps. For n>4 this results in a lower extinction efficiency. Figure 6(c) is a plot of the simulated extinction efficiency for normal

incidence excitation where the light electric field is aligned to the dipolar axes of symmetry in Figs. 4(b), 4(d), 4(g), and 4(h). This polarization excites the electric dipole mode of the system. Figure 6(c) is a plot of the extinction efficiency peak for the *n*=3-6 oligomers. Similar to the magnetic mode, the electric dipole also peaks at n=4, though the magnitude change is much smaller. Interestingly, for the oligomers that have an odd number of edges (n=3 and 5), do not have mirror symmetry along the axis perpendicular to the dipole and thus the extinction efficiency is lower than the equivalent even modes which have this mirror symmetry. Note that at normal incidence, the phase retardation does not excite the highest energy full antibonding mode.
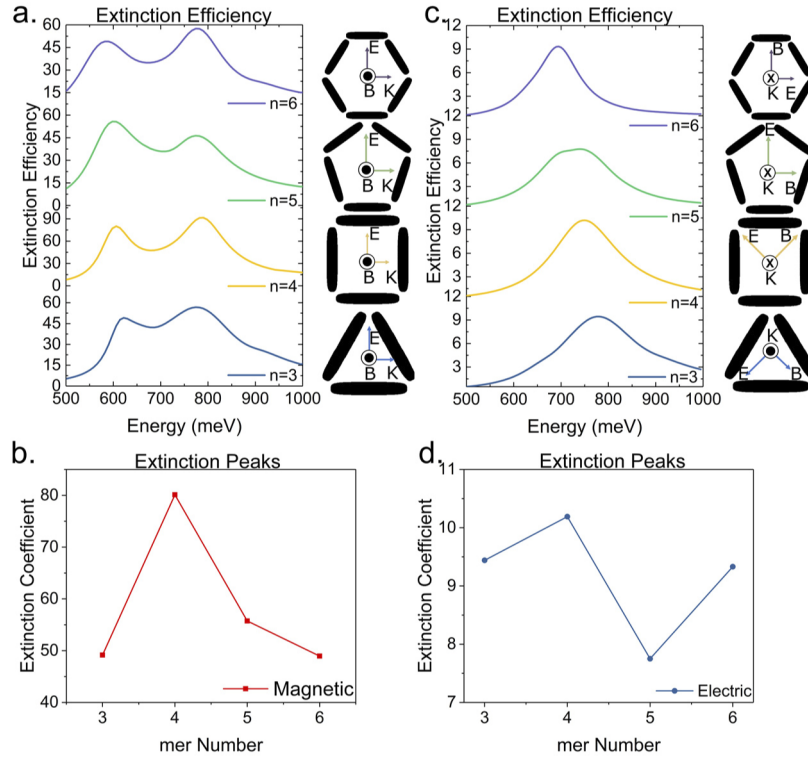

Fig. 6. a. Extinction efficiency spectra of a single rod and n=3-6 oligomers with the wave vector in the plane of the oligomer (note polarization next to each spectrum). b. Peak extinction efficiency values for the magnetic mode as a function of n. c. Extinction efficiency spectra of the electric dipole mode n=3-6 oligomers using normal incidence light (note polarization next to each spectrum). d. Peak extinction efficiency values for the electric dipole mode as a function of n.

In summary, we synthesize and characterize the hybridization of longitudinal dipole modes in nanorod oligomers with *n*=3-6 number of edges. High spatial and energy resolution EELS reveals that the splitting of the magnetic SPR mode and the SPR with maximum number of antibonding vertices increases with increasing number of edges. Intermediate modes for *n*>3 emerge where the energy ordering increases with increasing multipoles. Simulations of the EEL spectra agree well with the experimental spectra and SPR modes determined assuming the quasistatic limit, combined with multipole analysis, help reveal the symmetry/coupling of the nanorods in the oligomer. A study of the tetramer reveals that the energy splitting also increases with decreasing gap spacing and linearly blue-shifts with decreasing rod length. Finally, optical simulations show efficient magnetic coupling of the light field to the oligomers' magnetic modes, and for the dimensions studied here, the extinction efficiency has a maximum value in the extinction

efficiency for the *n*=4 arrangement. Furthermore, the full antibonding mode is also excited when optically excited with the wave vector aligned along the oligomer plane, which is attributed to phase retardation effects. When optically excited with normal incidence and the electric field aligned with the dipole mode, the extinction efficiency also peaks at the n=4 oligomer.

Disclosures. The authors declare no conflicts of interest

Supplemental document. See Supplement 1 for supporting content.

References

1. Y. Liu and X. Zhang, "Metamaterials: a new frontier of science and technology," Chem. Soc. Rev. **40**(5), 2494–2507 (2011).
2. J. Zhou, T. Koschny, M. Kafesaki, E. N. Economou, J. B. Pendry, and C. M. Soukoulis, "Saturation of the Magnetic Response of Split-Ring Resonators at Optical Frequencies," Phys. Rev. Lett. **95**(22), 223902 (2005).
3. F. Monticone and A. Alu, "The quest for optical magnetism: from split-ring resonators to plasmonic nanoparticles and nanoclusters," J. Mater. Chem. C **2**(43), 9059–9072 (2014).
4. N. Zohar, L. Chuntonov, and G. Haran, "The simplest plasmonic molecules: Metal nanoparticle dimers and trimers," J. Photochem. Photobiol., C **21**, 26–39 (2014).
5. D. W. Brandl, N. A. Mirin, and P. Nordlander, "Plasmon Modes of Nanosphere Trimers and Quadrumers," J. Phys. Chem. B **110**(25), 12302–12310 (2006).
6. S. Reich, N. S. Mueller, and M. Bubula, "Selection Rules for Structured Light in Nanooligomers and Other Nanosystems," ACS Photonics **7**(6), 1537–1550 (2020).
7. M. Hentschel, J. Dorfmüller, H. Giessen, S. Jäger, A. M. Kern, K. Braun, D. Zhang, and A. J. Meixner, "Plasmonic oligomers in cylindrical vector light beams," Beilstein J. Nanotechnol. **4**, 57–65 (2013).
8. Z.-J. Li, Z.-S. Wu, and H.-Y. Li, "Analysis of electromagnetic scattering by uniaxial anisotropic bispheres," J. Opt. Soc. Am. A **28**(2), 118–125 (2011).
9. N. Liu and H. Giessen, "Coupling effects in optical metamaterials," Angew Chem. Int. Ed. Engl. **49**(51), 9838–9852 (2010).
10. N. J. Greybush, V. Pacheco-Peña, N. Engheta, C. B. Murray, and C. R. Kagan, "Plasmonic Optical and Chiroptical Response of Self-Assembled Au Nanorod Equilateral Trimers," ACS Nano **13**(4), 3875–3883 (2019).
11. C. Cherqui, Y. Wu, G. Li, S. C. Quillin, J. A. Busche, N. Thakkar, C. A. West, N. P. Montoni, P. D. Rack, J. P. Camden, and D. J. Masiello, "STEM/EELS Imaging of Magnetic Hybridization in Symmetric and Symmetry-Broken Plasmon Oligomer Dimers and All-Magnetic Fano Interference," Nano Lett. **16**(10), 6668–6676 (2016).
12. M. A. Basyooni, A. M. Ahmed, and M. Shaban, "Plasmonic hybridization between two metallic nanorods," Optik **172**, 1069–1078 (2018).
13. F. Shafiei, F. Monticone, K. Q. Le, X.-X. Liu, T. Hartsfield, A. Alù, and X. Li, "A subwavelength plasmonic metamolecule exhibiting magnetic-based optical Fano resonance," Nat. Nanotechnol. **8**(2), 95–99 (2013).
14. J. A. Hachtel, A. R. Lupini, and J. C. Idrobo, "Exploring the capabilities of monochromated electron energy loss spectroscopy in the infrared regime," Sci. Rep. **8**(1), 5637 (2018).
15. O. L. Krivanek, T. C. Lovejoy, N. Dellby, T. Aoki, R. W. Carpenter, P. Rez, E. Soignard, J. Zhu, P. E. Batson, M. J. Lagos, R. F. Egerton, and P. A. Crozier, "Vibrational spectroscopy in the electron microscope," Nature **514**(7521), 209–212 (2014).
16. B. T. Draine and P. J. Flatau, "Discrete-Dipole Approximation For Scattering Calculations," J. Opt. Soc. Am. A **11**(4), 1491–1499 (1994).
17. N. W. Bigelow, A. Vaschillo, V. Iberi, J. P. Camden, and D. J. Masiello, "Characterization of the Electron- and Photon-Driven Plasmonic Excitations of Metal Nanorods," ACS Nano **6**(8), 7497–7504 (2012).
18. F. J. García de Abajo, "Optical excitations in electron microscopy," Rev. Mod. Phys. **82**(1), 209–275 (2010).
19. U. Hohenester and A. Trügler, "MNPBEM – A Matlab toolbox for the simulation of plasmonic nanoparticles," Comput. Phys. Commun. **183**(2), 370–381 (2012).
20. G. Boudarham and M. Kociak, "Modal decompositions of the local electromagnetic density of states and spatially resolved electron energy loss probability in terms of geometric modes," Phys. Rev. B **85**(24), 245447 (2012).
21. F. P. Schmidt, H. Ditlbacher, F. Hofer, J. R. Krenn, and U. Hohenester, "Morphing a Plasmonic Nanodisk into a Nanotriangle," Nano Lett. **14**(8), 4810–4815 (2014).

22. R. L. Olmon, B. Slovick, T. W. Johnson, D. Shelton, S.-H. Oh, G. D. Boreman, and M. B. Raschke, "Optical dielectric function of gold," Phys. Rev. B **86**(23), 235147 (2012).

23. K. Luke, Y. Okawachi, M. R. E. Lamont, A. L. Gaeta, and M. Lipson, "Broadband mid-infrared frequency comb generation in a Si3N4 microresonator," Opt. Lett. **40**(21), 4823–4826 (2015).

24. G. Guzzinati, A. Béché, H. Lourenço-Martins, J. Martin, M. Kociak, and J. Verbeeck, "Probing the symmetry of the potential of localized surface plasmon resonances with phase-shaped electron beams," Nat. Commun. **8**(1), 14999 (2017).

25. M. Zanfrognini, E. Rotunno, S. Frabboni, A. Sit, E. Karimi, U. Hohenester, and V. Grillo, "Orbital angular momentum and energy loss characterization of plasmonic excitations in metallic nanostructures in TEM," ACS Photonics **6**(3), 620–627 (2019).

26. S. C. Quillin, C. Cherqui, N. P. Montoni, G. Li, J. P. Camden, and D. J. Masiello, "Imaging plasmon hybridization in metal nanoparticle aggregates with electron energy-loss spectroscopy," J. Phys. Chem. C **120**(37), 20852–20859 (2016).

27. J. A. Fan, C. Wu, K. Bao, J. Bao, R. Bardhan, N. J. Halas, V. N. Manoharan, P. Nordlander, G. Shvets, and F. Capasso, "Self-Assembled Plasmonic Nanoparticle Clusters," Science **328**(5982), 1135–1138 (2010).

28. Y. Wu, Z. Hu, X.-T. Kong, J. C. Idrobo, A. G. Nixon, P. D. Rack, D. J. Masiello, and J. P. Camden, "Infrared plasmonics: STEM-EELS characterization of Fabry-Pérot resonance damping in gold nanowires," Phys. Rev. B **101**(8), 085409 (2020).